Quantum Computation Toolbox for Decoherence-Free Qubits Using Multi-Band Alkali Atoms

Mikhail Mamaev,* Joseph H. Thywissen, and Ana Maria Rey

Protocols for designing and manipulating qubits with ultracold alkali atoms in 3D optical lattices are introduced. These qubits are formed from two-atom spin superposition states that create a decoherence-free subspace immune to stray magnetic fields, dramatically improving coherence times while still enjoying the single-site addressability and Feshbach resonance control of state-of-the-art alkali atom systems. The protocol requires no continuous driving or spin-dependent potentials, and instead relies upon the population of a higher motional band to realize naturally tunable in-site exchange and cross-site superexchange interactions. As a proof-of-principle example of their utility for entanglement generation for quantum computation, it is shown that the cross-site superexchange interactions can be used to engineer 1D cluster states. Explicit protocols for experimental preparation and manipulation of the qubits are also discussed, as well as methods for measuring more complex quantities such as out-of-time-ordered correlation functions (OTOCs).

1. Introduction

The field of ultracold atomic physics in optical lattices has seen tremendous recent growth in its experimental implementations. There are many systems which feature unprecedented levels of cleanliness, environmental isolation, coherence time, and single-site addressability. These capabilities, especially the latter, have motivated recent experiments to apply optical lattice systems to the more ambitious goals of site-resolved quantum simulation[1] and quantum computation.[2] An ultracold atomic system realizing a quantum computer can offer the aforementioned benefits of coherence and isolation together with improved scalability, due to the number of atoms these systems can load simultaneously.

The prospect of quantum computing with ultracold neutral atoms has been explored in many contexts. These include the use of collisional gates,[3,4] collective states via cavity QED[5] or dipole blockade of atomic ensembles,[6] qubits encoded in vibrational atomic states,[7,8] spin-dependent lattices,[9] exchange[10,11] or spin-orbit coupled driving,[12] optical tweezers,[13,14] Rydberg atoms[15–17] and several others.[18] High-fidelity gates have been engineered using Rydberg atoms,[19–21] and targeted phase shifts.[22] Significant progress has also been made toward near-perfect initialization.[23–25] However, parallel generation of large entangled states remains an open challenge.

In this work we propose to use fermionic alkali atoms such as ^{40}K in 3D optical lattices to do initialization, state manipulation, and entanglement generation with logical qubits encoded in states generated by two atoms in two motional bands. Higher bands of optical lattices provide useful additional degrees of freedom,[26] and have been used for studies of superfluidity,[27–29] magnetism,[30,31] interferometry,[32] and interplay with collisional interactions.[33,34] Our logical qubits are designed to live in a decoherence-free subspace that resists unwanted effects of stray magnetic fields, leading to much longer coherence times[35,36] and accessibility to regimes utilizing stronger magnetic fields for dynamical control. We are further able to take advantage of the tunability of interactions via Feshbach resonances,[37–39] field gradients, and single-site resolution capabilities offered by state-of-the-art quantum gas microscopes[40–44] as powerful tools for qubit manipulation.
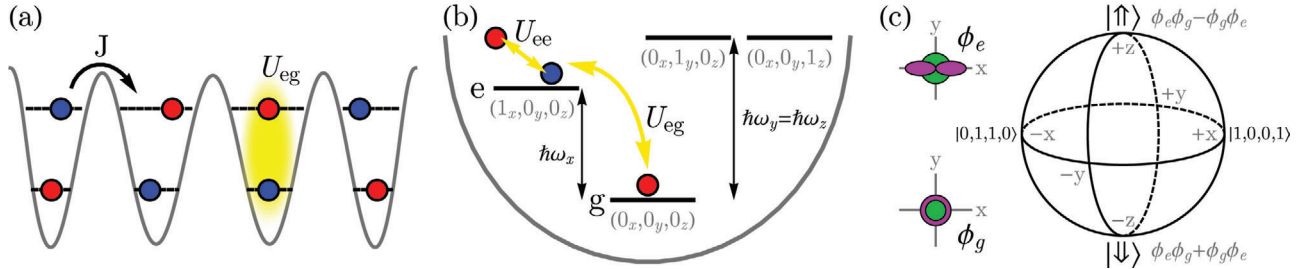
Our implementation makes use of the intra-band contact interactions as well as inter-band exchange interactions to implement logic qubit rotations and entanglement generation. We do not require continuous laser driving, nor any superlattice or spin-dependent lattice configurations. Through the additional use of a field gradient, we are able to tune the nearest-neighbor interactions between qubits to generate a desired Hamiltonian. As a proof-of-principle concept of measurement-based quantum computation[45,46] we show how to realize an Ising model with significantly stronger spin couplings compared to conventional superexchange, which we show can create high fidelity 1D cluster states. One can also tune the system to emulate XXZ or Heisenberg models, which may be used (as well as the Ising) to measure complex time-dependent quantities such as out-of-time-ordered correlation functions (OTOCs).[47,48] The interactions can be manipulated via Feshbach resonances, allowing us to turn them off and on as needed. The single-site resolution also permits the manipulation of individual atoms before and during such

M. Mamaev, Prof. A. M. Rey
JILA, NIST and Department of Physics
Center for Theory of Quantum Matter
University of Colorado
Boulder, CO 80309, USA
E-mail: mikhail.mamaev@colorado.edu
Prof. J. H. Thywissen
Department of Physics and CQIQC
University of Toronto
Ontario M5S 1A7, Canada

ADVANCED
SCIENCE NEWS

www.advancedsciencenews.com

ADVANCED
QUANTUM
TECHNOLOGIES

www.advquantumtech.com

Figure 1. a) Schematic of the optical lattice setup. Atoms can only tunnel along the *x* direction (effective 1D system). Each site holds two atoms (one per band), which exhibit intra-band repulsion and inter-band exchange interactions. b) Band schematic for a single lattice site. The atoms are loaded into the ground motional band *g*, and the first-excited band *e* with one motional excitation along the *x* direction. Other singly excited bands along *y*, *z* are not populated, and are nondegenerate with *e* due to higher lattice depths along *y*, *z*. Gray numbers in brackets are the harmonic excitation numbers, and ω_v for $v \in \{x, y, z\}$ are the on-site trapping frequencies. c) Effective Bloch sphere for the decoherence-free subspace. Logical 0 (1) states $|\Downarrow\rangle$ ($|\Uparrow\rangle$) are (anti-)symmetric superpositions of two different Wannier functions, with the opposite symmetry for the spin wavefunctions due to the overall fermionic nature of the atoms. Both these states are eigenstates of the interaction $\hat{H}_U$ and gradient $\hat{H}_B$, and are immune to uniform external magnetic fields.

computations, allowing for effective error detection and insight on what the quantum system is doing on a per-site basis.

In Section 2 we give an overview of our model, introduce the decoherence-free subspace used to define our logic qubits, and then derive the superexchange interactions between them. In Section 3 we detail how these interactions can be tuned through an external field gradient, and show how to use them for cluster state generation and OTOC measurement. In Section 4 we describe different protocols for qubit initialization and readout.

2. Decoherence-Free Subspace Qubits

2.1. Multi-Band Fermi-Hubbard Model

The system we work with is a 3D optical lattice populated by fermionic atoms, as depicted in **Figure 1**a. The atoms are prepared in their ground electronic state, and restricted to two populated hyperfine states which we denote as $\sigma \in \{\uparrow, \downarrow\}$ acting as a spin-1/2 degree of freedom. We assume the atoms are loaded into two motional bands *e* and *g*, with *e* an excited band holding one motional excitation along the *x* direction in the harmonic approximation (as shown in Figure 1b), and *g* the lowest band. The lattice depth is made more shallow along the *x* direction, confining the system to an effective 1D configuration. We assume a lattice with *L* lattice sites along the *x* direction, each one populated by two atoms (*N* atoms, *N* = 2*L*), one in *e* and one in *g*. The full Hamiltonian describing the system is a two-band Fermi-Hubbard model given by

$$\hat{H} = \hat{H}_J + \hat{H}_U + \hat{H}_B \tag{1}$$

where the tunneling Hamiltonian is

$$\hat{H}_J = -J \sum_{j,\sigma} \left(\hat{c}_{j,e,\sigma}^\dagger \hat{c}_{j+1,e,\sigma} + h.c. \right) \tag{2}$$

with $\hat{c}_{j,\mu,\sigma}$ annihilating an atom on site *j* in band $\mu \in \{e, g\}$ with spin σ. The lattice indexing is along *x* only. We have assumed that only *e*-band atoms can tunnel with rate *J*, and neglected any tunneling of *g*-band atoms. For the parameter regime of interest,

e-band tunneling is roughly 40 times faster due to the more delocalized nature of excited motional states. Since we will be working in the Mott-insulating regime, lowest-order tunneling dynamics will be second-order superexchange processes proportional to tunneling squared (hence $\sim 40^2$ times weaker for ground band tunneling).

The atoms also have an on-site interaction, whose Hamiltonian is

$$\hat{H}_U = \sum_j \left(U_{ee} \hat{n}_{j,e,\uparrow} \hat{n}_{j,e,\downarrow} + U_{gg} \hat{n}_{j,g,\uparrow} \hat{n}_{j,g,\downarrow} \right)$$

$$+ \frac{U_{eg}}{2} \sum_j \left(\hat{n}_{j,e,\uparrow} \hat{n}_{j,g,\downarrow} + \hat{n}_{j,e,\downarrow} \hat{n}_{j,g,\uparrow} \right)$$

$$- \frac{U_{eg}}{2} \sum_j \left(\hat{c}_{j,e,\uparrow}^\dagger \hat{c}_{j,e,\downarrow} \hat{c}_{j,g,\downarrow}^\dagger \hat{c}_{j,g,\uparrow} + h.c. \right) \tag{3}$$

where $\hat{n}_{j,\mu,\sigma} = \hat{c}_{j,\mu,\sigma}^\dagger \hat{c}_{j,\mu,\sigma}$. The first line is the interaction energy between atoms in the same band (U_{ee} and U_{gg} for *e* and *g* bands respectively), while the last two lines are direct and exchange interactions of strength U_{eg} between atoms in two different bands. The values for these interactions depend on the lattice depths, but their magnitudes can be globally tuned by using a Feshbach resonance to modify the scattering length. We will operate in the strongly interacting regime where $U_{ee}, U_{gg}, U_{eg} \gg J$. **Table 1** gives an overview of sample experimentally realistic parameters for a ^{40}K lattice; these are the parameters used in all plots throughout the paper unless otherwise specified. See Section A, Supporting Information, for details on the derivation of Equation (1) and its parameters.

In addition to the core lattice dynamics, we also permit an externally imposed linear field gradient along the *x* direction,

$$\hat{H}_B = \frac{B}{2} \sum_j j \times \left(\hat{n}_{j,e,\uparrow} - \hat{n}_{j,e,\downarrow} + \hat{n}_{j,g,\uparrow} - \hat{n}_{j,g,\downarrow} \right) \tag{4}$$

where *B* is the differential energy shift between sites. This shift could be implemented with a direct magnetic field gradient, or with the synthetic magnetic gradient of a vector light shift that

**ADVANCED
SCIENCE NEWS**
www.advancedsciencenews.com

**ADVANCED
QUANTUM
TECHNOLOGIES**
www.advquantumtech.com

Table 1. Sample system parameters for an optical lattice configuration using ^{40}K atoms. Here $E_r = h^2/(8ma^2) \approx h \times 4.5$ kHz is the recoil energy, using lattice spacing of $a = 527$ nm and mass of $m = 40$ amu. Interactions are computed using a scattering length of $a_s = 120a_0$ (with a_0 the Bohr radius). The value for a typical differential shift is chosen to give $B = |U_3| + 10J$.
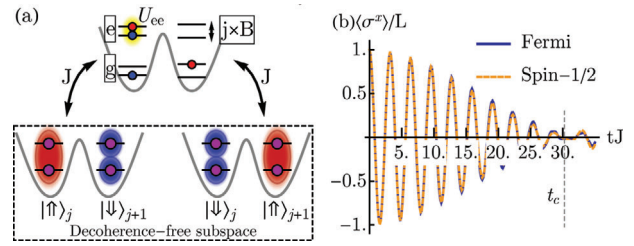
Parameter	Symbol	Value
Lattice depth	$(V_x, V_y, V_z)/E_r$	(40,60,60)
Excited band tunneling strength	J	$h \times 19$ Hz
Excited band repulsion	U_{ee}	$h \times 3.4$ kHz
Inter-band exchange interaction	U_{eg}	$h \times 4.5$ kHz
Ground band repulsion	U_{gg}	$h \times 4.7$ kHz
Superexchange energy denominators	$U_1 = 2U_{ee} + U_{eg}$	$h \times 11.3$ kHz
	$U_2 = 2U_{ee} - U_{eg}$	$h \times 2.2$ kHz
	$U_3 = 2U_{ee} - 3U_{eg}$	$-h \times 6.8$ kHz
Differential energy shift between sites	B	$h \times 7.0$ kHz
Superexchange spin model parmameters	$J_\parallel$	$h \times 0.47$ Hz
	$J_\perp$	$-h \times 0.51$ Hz
Cluster state generation time	t_c	260 ms

creates a differential potential between the two spin states. This gradient can modify the effective superexchange interactions between adjacent sites, providing a tuning parameter to manipulate the system dynamics. We do not model the effect of a common-mode (spin-independent) shift between sites; however, such a shift would provide an alternate tuning parameter to control the superexchange dynamics, as discussed below.

2.2. Decoherence-Free Subspace

The spin states σ feel different Zeeman shifts from external magnetic fields and are therefore vulnerable to uniform magnetic field fluctuations which severely reduce coherence times. To mitigate this effect, we use equal-weight superpositions of the spin states on every lattice site, which will feel no linear shift from an external magnetic field, thereby realizing a decoherence-free subspace.[35] These superpositions are the singlet and triplet states, $(|\uparrow, \downarrow\rangle \mp |\downarrow, \uparrow\rangle)/\sqrt{2}$ (written in first-quantized notation for two atoms on the same site). Their corresponding spatial wavefunctions must uphold the opposite symmetries to maintain overall fermionic parity, which can be accomplished by putting them in respective symmetric and anti-symmetric superpositions of the e, g band states, $(|e, g\rangle \pm |g, e\rangle)/\sqrt{2}$. The states for a single lattice site may thus be written as

$$
\begin{aligned}
|\Uparrow\rangle &= \frac{1}{2}\left(|\uparrow, \downarrow\rangle + |\downarrow, \uparrow\rangle\right)\left(|e, g\rangle - |g, e\rangle\right) \\
&= \frac{1}{\sqrt{2}}\left(|1, 0, 0, 1\rangle + |0, 1, 1, 0\rangle\right) \\
|\Downarrow\rangle &= \frac{1}{2}\left(|\uparrow, \downarrow\rangle - |\downarrow, \uparrow\rangle\right)\left(|e, g\rangle + |g, e\rangle\right) \\
&= \frac{1}{\sqrt{2}}\left(|1, 0, 0, 1\rangle - |0, 1, 1, 0\rangle\right)
\end{aligned}
\tag{5}
$$

Figure 2. a) Schematic for superexchange in the multi-band system. States in the decoherence-free subspace are coupled through a second-order virtual tunneling process by atoms in the e band. The intermediate state will have two atoms in the same band on the same site, exhibiting U_{ee} repulsion. Provided the energy gaps between the occupied and intermediate states are large compared to J, this leads to a spin-like interaction in the decoherence-free subspace. b) Benchmark comparison between the full Fermi–Hubbard model of Equation (1) and the superexchange model of Equation (8). The time t_c is the point where $\langle \hat{\sigma}^x \rangle$ vanishes, corresponding to the time needed to make a cluster state (see Section 3). Note that the oscillation frequency seen is not representative, and is an artifact of finite point sampling; the genuine oscillation frequency is set by U_{eg}.

where in the second lines of each equation we have rewritten the states in second quantization assuming a Fock basis ordering of $|n_{e,\uparrow}, n_{e,\downarrow}, n_{g,\uparrow}, n_{g,\downarrow}\rangle$. These states are also eigenstates of the interaction Hamiltonian,

$$
\begin{aligned}
\hat{H}_U |\Uparrow\rangle &= 0 \\
\hat{H}_U |\Downarrow\rangle &= U_{eg} |\Downarrow\rangle
\end{aligned}
\tag{6}
$$

and zero-energy eigenstates of the Zeeman Hamiltonian, $\hat{H}_B |\Uparrow\rangle = \hat{H}_B |\Downarrow\rangle = 0$. For experimentally realistic parameters (Table 1), the exchange interaction energy difference U_{eg} between these states can exhibit a > 100-fold reduction in sensitivity to external magnetic field fluctuations compared to the shifts that bare nuclear-spin states $\{e, g\}$ would experience.

Altogether, the decoherence-free states $\{|\Uparrow\rangle, |\Downarrow\rangle\}$ form a spin-1/2 logical qubit subspace on each site of the optical lattice, as shown in Figure 1c. We can have states along different axes of the associated Bloch sphere such as $|\Rightarrow\rangle = (|\Uparrow\rangle + |\Downarrow\rangle)/\sqrt{2} = |1, 0, 0, 1\rangle$ and $|\Leftarrow\rangle = (|\Uparrow\rangle - |\Downarrow\rangle)/\sqrt{2} = |0, 1, 1, 0\rangle$, which are maximally entangled between the spin and motional degrees of freedom. On-site qubit rotations can be made without leaving the subspace as discussed in Section 4. We are also robust to unwanted band-changing collisions into other singly excited bands (see Section E, Supporting Information), and to population of higher bands because of the 3D lattice band anharmonicity. Nearest-neighbor tunneling processes can be used to generate superexchange interactions and create entanglement between the qubits, as we will describe next.

2.3. Superexchange Hamiltonian

The single-site states in our decoherence-free subspace have energies of 0 or U_{eg} from the exchange interaction. However, if an e-band atom tunnels into an adjacent site, the resulting state will feel an intra-band U_{ee} interaction, as depicted in **Figure 2**a (U_{gg} plays no role as g atoms do not tunnel). So long as the energy difference between the configurations before and after tunneling

**ADVANCED
SCIENCE NEWS**

www.advancedsciencenews.com

**ADVANCED
QUANTUM
TECHNOLOGIES**

www.advquantumtech.com

is much larger than the tunneling amplitude J, no resonant tunneling will occur. However, the system will exhibit a second-order interaction through virtual processes starting and ending in the decoherence-free subspace, with an offresonant excited state in-between. This leads to an effective superexchange Hamiltonian $\hat{H}_{ex}$ between neighboring lattice sites[49,50] with matrix elements between states $|i\rangle$, $|j\rangle$ in the decoherence-free subspace given by

$$\langle i | \hat{H}_{ex} | j \rangle = \sum_k \Delta_{ijk} \langle i | \hat{H}_J | k \rangle \langle k | \hat{H}_J | j \rangle$$

$$\Delta_{ijk} = \frac{1}{2} \left(\frac{1}{E_i - E_k} + \frac{1}{E_j - E_k} \right)$$

(7)

where E_i is the unperturbed state energy $(\hat{H}_U + \hat{H}_B) | i \rangle = E_i | i \rangle$, and k runs over all excited states outside the decoherence-free subspace (see Section C, Supporting Information, for details). Note that we must also keep the unperturbed $\hat{H}_U + \hat{H}_B$ in the dynamics.

After some algebra, we find that the superexchange interaction takes the form of

$$\hat{H}_{ex} = J_\parallel \sum_j \hat{\sigma}_j^x \hat{\sigma}_{j+1}^x + J_\perp \sum_j \left(\hat{\sigma}_j^y \hat{\sigma}_{j+1}^y + \hat{\sigma}_j^z \hat{\sigma}_{j+1}^z \right)$$

$$+ J_{xz} \sum_j \left(\hat{\sigma}_j^x \hat{\sigma}_{j+1}^z - \hat{\sigma}_j^z \hat{\sigma}_{j+1}^x \right) + J_z \sum_j \hat{\sigma}_j^z$$

(8)

$$\approx \sum_j \left[\frac{J_\parallel + J_\perp}{2} \left(\hat{\sigma}_j^x \hat{\sigma}_{j+1}^x + \hat{\sigma}_j^y \hat{\sigma}_{j+1}^y \right) + J_\perp \hat{\sigma}_j^z \hat{\sigma}_{j+1}^z \right] + J_z \sum_j \hat{\sigma}_j^z$$

Here, $\hat{\sigma}_j^\nu$ are standard Pauli operators acting on the $\{|\Uparrow\rangle, |\Downarrow\rangle\}$ logic qubits at site j. The coefficients depend on three particular combinations of the repulsive and exchange interactions that show up in the energy denominators of Equation (7),

$$U_1 = 2 U_{ee} + U_{eg}$$

$$U_2 = 2 U_{ee} - U_{eg}$$

(9)

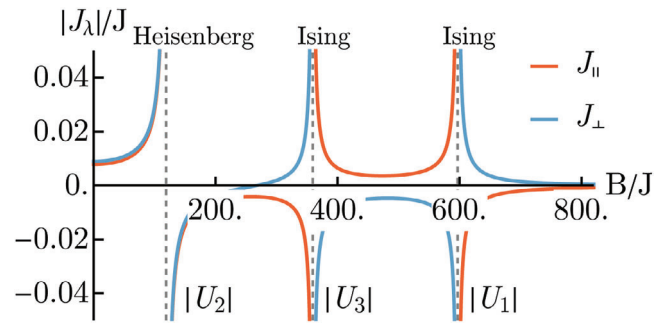$$U_3 = 2 U_{ee} - 3 U_{eg}$$

The corresponding coupling constants are

$$J_\parallel = -\frac{J^2}{2} \left(\frac{U_1}{B^2 - U_1^2} + \frac{2 U_2}{B^2 - U_2^2} + \frac{U_3}{B^2 - U_3^2} \right)$$

$$J_\perp = \frac{J^2 U_2 (3 B^2 + U_1 U_3)(U_1 - U_2)^2}{(B^2 - U_1^2)(B^2 - U_2^2)(B^2 - U_3^2)}$$

$$J_{xz} = -\frac{2 B J^2 U_2 (U_1 - U_2)}{(B^2 - U_1^2)(B^2 - U_2^2)}$$

(10)

$$J_z = J^2 \left(\frac{U_1}{B^2 - U_1^2} - \frac{U_3}{B^2 - U_3^2} \right) - \frac{U_1 - U_2}{4}$$

Table 1 shows these derived values for experimentally realistic setups.

Figure 3. Field gradient dependence of the superexchange interaction parameters $J_\parallel$ and $J_\perp$, using the parameters in Table 1 (except B). All of the resonance points where $B = |U_\gamma|$ for $\gamma \in \{1, 2, 3\}$ are marked with dashed lines.

Note that in going to the second line of Equation (8), we have used the fact that the external field $\sim J_z \hat{\sigma}^z$ imposed by the bare exchange interactions [i.e. the $(U_1 - U_2)/4$ in J_z coming from $\hat{H}_U$] is much larger than any superexchange processes. As a result, some of the terms in the first two lines of Equation (8) can be neglected. To a good approximation, the system is projected into a given $\hat{\sigma}^z$-eigenvalue manifold, causing the J_{xz} term to be negligible in a rotating-wave approximation. Furthermore, any $\hat{\sigma}^x \hat{\sigma}^x$ or $\hat{\sigma}^y \hat{\sigma}^y$ terms will be projected into a $(\hat{\sigma}^+ \hat{\sigma}^- + h.c.)$ form. This allows us to recollect them and write the Hamiltonian as an effective XXZ-type model with an external field.

This model is valid so long as all of the denominators are large compared to the tunneling, that is, $|B - |U_\gamma|| \gg J$ for $\gamma \in \{1, 2, 3\}$, to avoid higher-order effects. Figure 2b shows a comparison between the full Fermi–Hubbard dynamics and the superexchange model, looking at collective observable $\langle \hat{\sigma}^x \rangle = \sum_j \langle \hat{\sigma}_j^x \rangle$ (Section 4 discusses its measurement).

3. Entanglement Generation

3.1. Interaction Form

While the form of the interaction coefficients in our superexchange model is nontrivial, the key features are the non-identical denominators. By tuning the parameters such that some of the denominators become much smaller than the others, we can choose which interactions get turned on and off. This permits the isolation of terms of interest, which can then be employed for useful entanglement generation.

Figure 3 plots $J_\parallel$ and $J_\perp$ as a function of field gradient B (assuming $B > 0$). We observe three resonances, where $B = |U_\gamma|$ for some γ and the corresponding denominator vanishes. While our second-order perturbative Hamiltonian will not be correct at those resonance points due to higher-order effects, if we stay close to them while still obeying $|B - |U_\gamma|| \gg J$, the superexchange Hamiltonian will remain valid and the near-resonant terms will dominate the dynamics.

Operating close to the resonance conditions $B \approx |U_3|$ or $B \approx |U_1|$ is of particular utility since in this case, $J_\parallel \approx -J_\perp$ and

ADVANCED
SCIENCE NEWS

www.advancedsciencenews.com

ADVANCED
QUANTUM
TECHNOLOGIES

www.advquantumtech.com

to leading order the $\hat{\sigma}^x\hat{\sigma}^x + \hat{\sigma}^y\hat{\sigma}^y$ terms are cancelled out. We are left with just an Ising model,

$$\lim_{B\to|U_3|,|U_1|}\hat{H}_{ex} = J_{zz}\sum_j \hat{\sigma}_j^z\hat{\sigma}_{j+1}^z + J_z\sum_j \hat{\sigma}^z \tag{11}$$

where $J_{zz} \approx J_\perp \approx -J_\parallel$. Since we cannot be exactly at resonance, there will be some discrepancy between the two coefficients; a sufficient approximation is to take the average, $J_{zz} \approx (J_\perp - J_\parallel)/2$. The nearest-neighbor Ising model has a wide variety of applications for entanglement generation between qubits, and can be used to make cluster states as demonstrated in the next section. Furthermore, the Ising interaction strength near the resonance scales as $\sim J^2/|B - |U_\gamma||$, which is much faster than conventional superexchange $\sim J^2/U_\gamma$ (the former's denominator is on the order of $\sim 10J$, while the latter is $\sim 100J$).

The system's tunability also permits realization of other spin models. If we instead bring the field gradient close to the $|U_2|$ resonance, the interaction coefficients are equal in magnitude and sign, which creates a Heisenberg model with a transverse field:

$$\lim_{B\to|U_2|}\hat{H}_{ex} = J_\perp\sum_j \vec{\sigma}_j\cdot\vec{\sigma}_{j+1} + J_z\sum_j \hat{\sigma}^z \tag{12}$$

Finally, as seen from Equation (8), we can realize the XXZ model with a wide range of coefficients, which has seen recent experimental interest.[51]

The homogeneity (how close $|J_\parallel|$ can be made to $|J_\perp|$) and positions of the resonance points depend on the interaction strength. Having higher U_{ee}/J, U_{eg}/J leads to better homogeneity, but at the cost of moving the resonance points outward and thus requiring a larger field gradient B/J. This requirement can be mitigated by reducing the tunneling rate J, implying a compromise between gradient strength and experimental timescale. Increasing U_{ee}, U_{eg} without affecting J is done by either increasing transverse lattice depth along the y, z directions or increasing the scattering length a_s via Feshbach resonance.

3.2. Cluster State Generation

The Ising model in Equation (11) can be employed to generate useful entanglement for quantum computation. We can generate a cluster state, which is a multipartite entangled state used for measurement-based quantum computing.[45] A cluster state is a resource that can reproduce the results of circuit-based computations without needing explicit entangling gates between individual qubits. All entanglement generation is front-loaded into the cluster state itself. Once this state is prepared, a computation is done by successive feed-forward measurements. Given the long coherence times and innate 3D nature of the lattice, we can not only generate a single cluster state, but an entire array of them to be used or sorted as needed. While a 1D cluster state alone is not sufficient for universal computation, our protocol can be extended to 2D in a straightforward manner as discussed in Section 5. We focus on 1D as a proof-of-principle demonstration of the system's capabilities.

A cluster state is defined as

$$|\psi_c\rangle = \prod_j \exp\left[-i\frac{\pi}{4}\left(\hat{\sigma}_j^z\hat{\sigma}_{j+1}^z - \hat{\sigma}_j^z - \hat{\sigma}_{j+1}^z\right)\right]|\psi(0)\rangle \tag{13}$$

where the exponential operator is a controlled phase gate, applied across all nearest-neighbor links. The initial-state corresponds to a spin-polarized state along $+x$,

$$|\psi(0)\rangle = \prod_j |\Rightarrow\rangle_j \tag{14}$$

As seen from Equation (11), our system already contains the necessary Ising interaction. The protocol we use is similar to the one discussed in ref. [12], but without the need for continuous laser driving and easier to tune with the field gradient. We simply prepare the initial state $|\psi(0)\rangle$ (as described in Section 4), quench the field gradient or interaction strength (via Feshbach resonance) to satisfy $B \approx |U_3|$, and wait for a time

$$t_c = \pi/(4J_{zz}), \quad J_{zz} \approx (J_\perp - J_\parallel)/2 \tag{15}$$

This will implement the cross-site terms in the controlled phase gate. The only remaining task is to implement the single-particle terms. Since our J_z is so much larger than the interaction and commutes with it (to good approximation), we could in principle determine how many full periods of single-particle evolution have occurred during t_c, and then compensate by letting the system evolve further such that the total time spent is $\pi/(2J_z) \mod \pi/J_z$. However, a more prudent approach is to use a spin-echo π pulse $\hat{\Pi} = e^{-i\pi\hat{\sigma}^x/2}$ halfway through the evolution. This will cause any phase accrued from the single-particle terms to be undone by itself during the second half of the evolution. In addition, such a pulse can help with unwanted sources of noise that are not captured by our model. After this evolve-echo-evolve sequence is done, we let the system evolve further for a time $\pi/(2J_z)$ for the necessary single-particle rotation, and then stop the dynamics by turning off the tunneling and interactions (via Feshbach resonance). The overall protocol is thus,
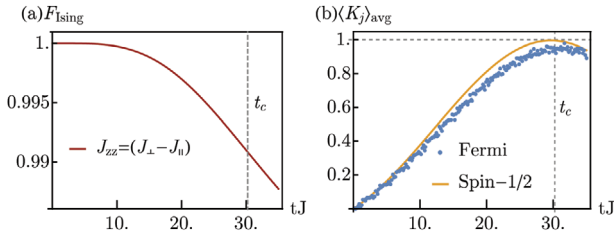
$$|\psi_c\rangle = e^{-i\hat{H}_{ex}\pi/(2J_z)}e^{-i\hat{H}_{ex}t_c/2}\hat{\Pi}e^{-i\hat{H}_{ex}t_c/2}|\psi(0)\rangle \tag{16}$$

Figure 4a shows state fidelity between time-evolution using the echo protocol with our superexchange model of Equation (8) and an ideal Ising model evolution which can generate a perfect cluster state. Inhomogeneity between $J_\parallel$ and $J_\perp$ and the breakdown of the rotating-wave approximation (since J_z is not infinite) are the main sources of error, but in general they can be made small.

One of the core advantages to measurement-based quantum computation is that the quality of a cluster state can be estimated using spatially local properties rather than global fidelity. To this end, we look at multi-body correlators called stabilizer operators, defined as

$$\hat{K}_j = \hat{\sigma}_j^x \prod_{i\in\{j-1,j+1\}} \hat{\sigma}_i^z \tag{17}$$

i.e. products of an $\hat{\sigma}^x$ measurement on one site and $\hat{\sigma}^z$ on all its neighbouring sites (thus a three-body operator in 1D, 5 in 2D,

**ADVANCED
SCIENCE NEWS**

www.advancedsciencenews.com

**ADVANCED
QUANTUM
TECHNOLOGIES**

www.advquantumtech.com

Figure 4. a) Fidelity between the state generated by the spin-echo protocol of Equation (16), and the state generated by an ideal Ising model with $J_{zz} = (J_\perp - J_\parallel)/2$. System size is $L = 8$. b) Stabilizer values $\langle \hat{K}_j \rangle$ for the spin-echo protocol using the superexchange model $\hat{H}_{ex}$ (orange line) and full Fermi-Hubbard model $\hat{H}$ (blue dots), for system size $L = 4$. The stabilizer operators in the corners are defined differently: The missing $\hat{\sigma}_j^z$ is absent from the correlator, and an overall rotation of $e^{-i\pi\hat{\sigma}^z/4}$ is applied to the state before calculating them, since they are missing such a rotation from the vacant link on the open end.

and 7 in 3D). An ideal cluster state is an eigenstate of all such stabilizer operators with eigenvalue 1,

$$\hat{K}_j |\psi_c\rangle = + |\psi_c\rangle, \quad \langle \psi_c| \hat{K}_j |\psi_c\rangle = +1 \tag{18}$$

Note that the sign of the eigenvalue does not matter as long as it is the same for all sites, since we can flip it by applying a collective $\hat{\sigma}^z$ rotation. The closeness of each stabilizer correlator $\langle \hat{K}_j \rangle$ to 1 serves as a local measure of cluster state quality. If we average it over a region of the lattice, $\langle \hat{K}_j \rangle_{avg} = \sum_j \langle \hat{K}_j \rangle$, we get an estimate of the fidelity for computations done using that region.

Figure 4(b) shows the average value of these cluster correlators for a small system as our protocol goes on. Note that in our simulations the lattice has boundaries, which means that the corner sites have their respective stabilizer operators defined differently (see caption). The main deviations come from inhomogeneity between $J_\parallel$ and $J_\perp$, as well as leakage of population into the excited states due to higher-order processes. These can be remedied by driving further from resonance (at the cost of longer t_c), and using larger interactions to keep the coefficients homogeneous (at the cost of needing a stronger gradient). However, we still find high stabilizer values $\langle \hat{K}_j \rangle_{avg} > 0.95$ indicating a good cluster state.

3.3. OTOC Measurement

Another powerful feature of the tunable superexchange coefficients (see Figure 3) is their ability to change sign. We can quench the gradient from just below one of the resonances, say $B \lesssim |U_3|$, to just above, $B \gtrsim |U_3|$. This flips the interaction coefficient, allowing for the implementation of a unitary time-reversal. Such capabilities are applicable to the study of out-of-time ordered correlation functions (OTOCs), which have garnered much recent interest due to their applications in quantum chaos, butterfly effects and temporal correlation spreading.[48]

An OTOC is a two-time, four-operator correlator defined as $\langle \hat{W}^\dagger(t) \hat{V}^\dagger \hat{W}(t) \hat{V} \rangle$, where $\hat{W}$, $\hat{V}$ are time-independent commuting operators and $\hat{W}(t) = e^{i\hat{H}t} \hat{W} e^{-i\hat{H}t}$. The connection to chaos can be understood by considering $\hat{W}$, $\hat{V}$ to be local operators with some spatial separation. When the system is initialized, they commute
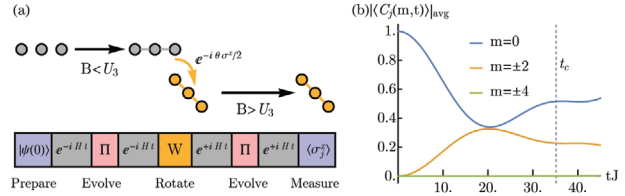
Figure 5. a) Schematic of the OTOC-measuring protocol of Equation (19). The sign of the Hamiltonian is changed by quenching the field gradient B from below to above a resonance (here the $|U_3|$ resonance), choosing the $J_\perp$ values to have equal magnitude and opposite sign. π pulses are done in the middle of each evolution to remove unwanted single-particle rotations. b) Fourier-transformed OTOC components [see Equation (21)], averaged over all j and computed with the superexchange model. System size is $L = 8$ (open boundaries). Parameters are from Table 1 with the magnetic field quenched from $B/J = 350$ to $B'/J = 370$ about the $|U_3|/J = 359$ resonance, corresponding to $J_\perp/J = \pm 0.025$.

and the corresponding OTOC is zero. As correlations spread, the spatial extent of $\hat{W}$ and thus the OTOC increase. The slope of increase gives information about the propagation of correlations in the system.

In our case, we can measure an OTOC in a straightforward manner. We time-evolve under the effective superexchange Hamiltonian to a time t, apply a spin rotation by some angle θ, quench the field gradient to flip the interaction sign, evolve for another t, and finally measure some observable (total evolution time $2t$), similar to the sequence used in ref. [52]. If we start in $|\psi(0)\rangle$, a sample such protocol may be written as

$$
\begin{aligned}
\langle \hat{C}_j(\theta, t) \rangle &= \langle \psi(0)| \left(e^{+i\hat{H}_{ex}t} e^{-i\frac{\theta}{2}\hat{\sigma}^x} e^{-i\hat{H}_{ex}t} \right) \\
&\quad \hat{\sigma}_j^x \left(e^{+i\hat{H}_{ex}t} e^{-i\frac{\theta}{2}\hat{\sigma}^x} e^{-i\hat{H}_{ex}t} \right) |\psi(0)\rangle \\
&= \langle \psi(0)| \hat{W}^\dagger(t) \hat{V}^\dagger \hat{W}(t) \hat{V} |\psi(0)\rangle
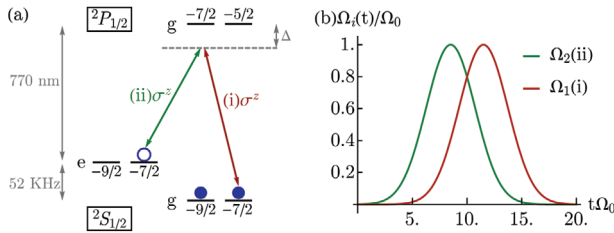\end{aligned}
\tag{19}
$$

where $\hat{W} = e^{-i\frac{\theta}{2}\hat{\sigma}^x}$, and $\hat{V} = \hat{\sigma}_j^x$. In going to the second line, we have used the fact that $\hat{\sigma}_j^x |\psi(0)\rangle = |\psi(0)\rangle$. **Figure 5**a depicts this protocol.

The sign change can be done about any $|U_\gamma|$ resonance (see Figure 3). Here we will use the Ising model with $|U_3|$. Note that each half of the time-evolution will also include a spin-echo midway to remove the $\hat{\sigma}^z$ single-particle rotations, since their sign cannot be fully reversed. The total implementation is thus,

$$
\begin{aligned}
e^{-i\hat{H}_{ex}t} &= e^{-i\hat{H}_{ex}(B)t/2} \hat{\Pi} e^{-i\hat{H}_{ex}(B)t/2} \\
e^{+i\hat{H}_{ex}t} &= e^{-i\hat{H}_{ex}(B')t/2} \hat{\Pi} e^{-i\hat{H}_{ex}(B')t/2}
\end{aligned}
\tag{20}
$$

with B, B' on opposite sides of the chosen resonance, set such that the magnitude of J_{zz} is equal for both. For the parameters of $U_1/J = 597$, $U_2/J = 119$, $U_3/J = -359$ (from Table 1), we can quench the gradient about the $|U_3|$ resonance from $B/J = 350$ to $B'/J = 370$, yielding effective interaction strengths of $J_\perp/J \approx \pm 0.025$.

We can measure different OTOCs depending on evolution time t and rotation angle θ. For $\theta = 0$, we have trivial unitary reversal, and the corresponding OTOC would be equal to unity. As

**ADVANCED
SCIENCE NEWS**

www.advancedsciencenews.com

**ADVANCED
QUANTUM
TECHNOLOGIES**

www.advquantumtech.com

Figure 6. a) Raman scheme for transferring an ↑ atom to the e band. Two linearly polarized lasers (i) and (ii) couple the states $|{}^2S_{1/2}, g; 9/2, -7/2\rangle$ and $|{}^2S_{1/2}, e; 9/2, -7/2\rangle$ through an excited state $|{}^2P_{1/2}, g; 7/2, -7/2\rangle$ (transition wavelength ≈ 770 nm, unpopulated due to large detuning) with single-photon Rabi frequencies of Ω_1 and Ω_2 respectively. Here the state label is $|\Lambda, \mu; F, m_F\rangle$, with electronic state Λ, band μ, nuclear-spin F and projection m_F (see Supporting Information for details). A π pulse effects the coherent transfer. b) STIRAP scheme for the same transfer. Instead of always-on constant Rabi frequencies for both lasers, we first ramp up Ω_2 coupling the initially unoccupied states with a Gaussian profile, then ramp it down while ramping up Ω_1. The state is adiabatically dragged into the desired configuration. Here Ω_0 is the maximum Rabi frequency the lasers reach, equal for both.

the angle increases, the OTOC exhibits a decaying slope as correlations build up. Another useful piece of information that can be extracted is the spectral fourier transform of the OTOCs,

$$\langle \hat{C}_j(m,t)\rangle = \sum_\theta e^{im\theta}\langle \hat{C}_j(\theta, t)\rangle \tag{21}$$

where $\theta = \frac{2\pi n}{L}$ and $n, m \in \{0, \dots, L-1\}$. The different m components give information about the system's connectivity.[52] In a 1D lattice with two neighbours per site, we should see signals at $m = \pm 2$. A 2D lattice would have signals at $\pm 4, \pm 2$, and a 3D lattice at $\pm 6, \pm 4, \pm 2$. Figure 5b shows these fourier-transformed OTOC values for our superexchange model. Note that we do not see any special peak or trough at $t = t_c$ because our system has open boundaries, and thus the OTOCs will feel edge effects since we average over every site. However, site-resolved OTOCs can be probed in this system with a quantum gas microscope.

4. Preparation and Control Tools

4.1. State Preparation

In this section, we detail an explicit experimental protocol for preparing atoms in the required decoherence-free subspace. The starting point is a band insulator (two atoms of opposite spin per site) in the lowest band g, which can be prepared by standard cooling techniques.[53–55] We then use a Raman scheme to selectively drive one of the atoms (the spin-↑ one) into the e band. The result is a state of the form $|1, 0, 0, 1\rangle = |\Rightarrow\rangle$ on every site, which can immediately be used for cluster state generation. One can also rotate this state into others using the protocols of the next section.

The process is depicted in **Figure 6**a. We use a linearly polarized laser pair to couple an occupied state in the g band to an empty target state in the e band via an intermediate excited state in a higher electronic level. The laser detunings Δ from the excited state are chosen to be equal and large compared to their Rabi frequencies Ω_1, Ω_2, creating a Raman coupling $\Omega = \Omega_1\Omega_2/\Delta$

between the occupied and target states. The other first-excited bands along y or z do not participate because of their energy shift due to unequal lattice depth. Doing a π pulse implements a coherent transfer, populating the e band with one ↑ atom. See Section B, Supporting Information, for more details.

We note that the speed at which this transfer can be made is limited by the energy gaps to other unwanted bands, which we do not want to populate. The two-photon Rabi frequency Ω must be small compared to all gaps to other excited bands. The lowest of these gaps is an unwanted coupling from first-excited band state $e = (1, 0, 0)$ to the second-excited state $(2,0,0)$, which is offresonant from the $(0, 0, 0) \leftrightarrow (1, 0, 0)$ transition we use by ≈ 5 kHz. On the other hand, Ω should also be faster than any intrinsic decoherence processes to ensure that state preparation can be done before the model breaks down. Finally, the detuning Δ must be larger than spontaneous decay rate in the intermediate state. All of the above requirements can be met by first making the detuning Δ sufficiently large, then providing enough laser power (increasing Ω_1, Ω_2) to make Ω satisfy the desired intermediate regime.

If a coherent π pulse with the above setup poses experimental challenges, one may instead use a STIRAP protocol.[56,57] The laser configurations are the same, but instead we slowly ramp the laser intensities with offset Gaussian profiles as depicted in Figure 6b. The coupling between the initially unoccupied states [laser (ii)] is counter-intuitively ramped up first, and then the coupling between the initially occupied and excited states [laser (i)] is ramped up while the previous coupling is reduced. The system follows an adiabatic evolution where the ground-state is transferred into a final configuration with the atom in the target state. Unlike the previous protocol, STIRAP can function even with $\Delta = 0$, and enjoys better robustness to laser noise or bandwidth limitations.

4.2. Rotations

Quantum computation requires readily accessible rotations upon the qubits in the decoherence-free subspace. A $\hat{\sigma}^z$-type rotation is straightforward because the exchange interaction creates such a term implicitly. We tune U_{eg} to be large enough for fast rotations and far from any resonances, then wait the desired time. On-site rotations of this type can be implemented with a focused laser to change the lattice potential (and thus interactions) that a site feels.

A $\hat{\sigma}^x$ rotation may be realized with differential Stark shifts. The desired rotation operator takes the form of $|1, 0, 0, 1\rangle \langle 1, 0, 0, 1| - |0, 1, 1, 0\rangle \langle 0, 1, 1, 0|$ in the Fock basis, which can be implemented by energetically shifting one of the $\{|\Rightarrow\rangle, |\Leftarrow\rangle\}$ states in the decoherence-free subspace (i.e. applying a $\hat{\sigma}^z$ rotation in the $\{|1, 0, 0, 1\rangle, |0, 1, 1, 0\rangle\}$ basis). This may be done with a laser such as (i) in Figure 6a. The detuning Δ is set sufficiently large compared to the single-photon laser Rabi frequency Ω_1 that no population transfer occurs; the lowest-order effect is then to shift the state $|1, 0, 0, 1\rangle$ by Ω_1^2/Δ, realizing the desired rotation up to an identity term in the Hamiltonian. While in general one would need to avoid perturbing the e state (separated from g by ~ 52 kHz gap) via transition (ii) in Figure 6a, this requirement may be achieved through symmetry. The laser (ii)

ADVANCED
SCIENCE NEWS
www.advancedsciencenews.com

ADVANCED
QUANTUM
TECHNOLOGIES
www.advquantumtech.com

matrix element normally vanishes due to the spatial symmetry of the wavefunctions about the lattice site center (see Section B, Supporting Information). For state preparation, we avoid this by aiming laser (ii) along the x direction, which introduces an additional phase to break the symmetry and prevents the integral from vanishing. For rotations, if we aim laser (i) along y or z instead, transition (ii) will have a vanishing overlap integral, allowing us to generate the desired rotation. For collective rotations such as the π pulse in the cluster state protocol, we can even use the same beam as the one used in state preparation. We may need to have interactions U_{eg} turned off to avoid rotating about multiple axis simultaneously, but this can also be done without having to ramp Feshbach fields by adjusting the light shifts.

A $\hat{\sigma}^x$ rotation may also be realized by using additional external ingredients. One method is an on-site field gradient. A linear gradient is no longer sufficient, because it has no on-site effect on the decoherence-free subspace (see Section D, Supporting Information). While a linear gradient was used to tune the cross-site superexchange interactions, there it only shifted the energies of the states involved: adjacent qubits are tunnel-coupled. For direct coupling between the decoherence-free states, a quadratic field variation is required. For example, an effective magnetic curvature could be realized via state-dependent optical potentials for the bare spin states σ using the differential magnetic moments and vector Stark shifts. One could also apply a magnetic field curvature directly. The Hamiltonian for such a gradient on a site j is,

$$\hat{H}_{\delta B} = \delta\Omega(x - x_0)^2\left(\hat{n}_{j,\uparrow} - \hat{n}_{j,\downarrow}\right) \tag{22}$$

where the gradient is along the tunneling direction x, focused near one lattice site and centered about some position x_0. Evaluating the effect of this gradient for a single site (see Section D, Supporting Information), we arrive at the following Hamiltonian in the basis $\{|\Uparrow\rangle, |\Downarrow\rangle\}$ (on site j):

$$\hat{H}_{\text{site}} = \begin{pmatrix} 0 & \frac{\hbar\,\delta\Omega}{m\omega_x} \\ \frac{\hbar\,\delta\Omega}{m\omega_x} & U_{eg} \end{pmatrix} = -\frac{U_{eg}}{2}\hat{\sigma}^z_j + \frac{\hbar\,\delta\Omega}{m\omega_x}\hat{\sigma}^x_j \tag{23}$$

A $\hat{\sigma}^x$ rotation may be done by either turning the interactions off via Feshbach resonance, or ensuring that $\hbar\,\delta\Omega/(m\omega_x) \gg U_{eg}$. For most cases, the former will be the better choice as we do not want arbitrary on-site exchange interactions acting on the qubits unless we are generating a cluster state. One could also overcome the U_{eg} interactions with a high $\delta\Omega$; while this would need a very strong field gradient, having such a requirement also shows a degree of robustness to unwanted magnetic curvature (see discussion in Section D, Supporting Information).

4.3. Readout

The final required piece of the toolbox is to measure the qubits in the decoherence-free subspace. Measurements of the $\hat{\sigma}^x$ component can be done by simply reversing the state preparation protocol, then measuring the occupation of the g band. If the qubit was in $|\Rightarrow\rangle$ we would find two atoms, and if in $|\Leftarrow\rangle$, we would find one, offering a simple metric.

The $\hat{\sigma}^z$ component is more complex, but can be avoided altogether because we have access to rotations about two axes. We first rotate by $\pi/2$ about the x axis on the Bloch sphere, then by $\pi/2$ about the z axis, and finally measure $\hat{\sigma}^x$. If we were in $|\Uparrow\rangle$ we would end up in $|\Rightarrow\rangle$ and find two atoms, whereas the $|\Downarrow\rangle$ state would be rotated into $|\Leftarrow\rangle$ and yield one.

We note that for the more complex application of doing quantum computation with a cluster state, one requires sequential site-resolved measurements that do not cause destructive effects on adjacent lattice sites. There are several protocols in current-generation optical lattice systems which can provide such desired capabilities. One option is an accordion-type lattice[58] that expands the lattice spacing a without changing the confining laser wavelength, which can be used after the cluster state is generated to spread the atoms out and permit site-resolved measurement with focused beams. Another option is a local transition of a single lattice site into a different hyperfine state, which can be selectively measured.[59] While there can be detrimental effects to adjacent sites due to insufficient beam focusing, frequency selection on the desired site should allow the damage done to the others to remain coherent, making it possible to undo the crosstalk with a suitable laser pulse after each measurement.

5. Conclusions

We have proposed protocols for using 3D optical lattices populated by atoms in higher bands to realize qubits for quantum computation. Our design embeds the logical states in a decoherence-free subspace, which greatly amplifies the system coherence time while still having scalability, single-site addressability and tunable interactions via Feshbach resonances and electromagnetic field control. State preparation and on-site rotations can be implemented with Raman transitions and external field gradients, allowing for straightforward manipulation of qubit states. Superexchange interactions between the qubits can also be tuned in form and amplitude with field gradients, allowing (among other things) the generation of an Ising model useful for cluster state generation and OTOC measurement.

This system has an abundance of natural extensions that can be implemented without significant modifications to the protocols. While our design allows the creation of a 1D cluster state, 2D states can be generated by reducing the tunneling along y and inducing superexchange dynamics along that direction as well (still keeping the lattice depth sufficiently different from x so that unwanted band-changing collisions do not occur). Since the dynamics are controlled by a field gradient, we can enable or disable interactions at will, allowing us to build the cluster state up one dimension at a time as the controlled phase gate operations commute. Such a state allows for universal computation using measurement-based protocols. Furthermore, if we seek to study OTOCs, we can use locally applied fields to induce local perturbations and measure their propagation directly on a site-to-site basis rather than relying upon collective observables.

While our protocols have been described for alkali atoms, straightforward extensions can also be made to systems using alkaline earth atoms instead. The higher-band configuration can be mimicked through the use of different electronic states (with the g, e bands replaced by, e.g., ground and excited clock states,

**ADVANCED
SCIENCE NEWS**

www.advancedsciencenews.com

**ADVANCED
QUANTUM
TECHNOLOGIES**

www.advquantumtech.com

while the bare spin σ remains represented by hyperfine states). The resulting system would still exhibit both inter- and intra-state interactions for the two electronic states. Applying an electronic-state dependent lattice intensity can likewise restrict tunneling to just one of the two electronic states, reproducing our proposed setup. Alkaline earth atoms can provide additional stability and robustness due to their naturally high coherence times and magnetic field insensitivity. Related prospects, including the use of decoherence-free subspaces, have been explored in refs. [60, 61].

Other possible applications for our proposed setup include the generation of other useful entangled states such as spin-squeezed states,[62] by generating appropriate XXZ-type Hamiltonians[63,64] or similar gap-protected spin interactions.[65,66] The restrictions on motion due to the use of higher bands can lead to exotic spatially correlated physics mimicking spin-orbit coupled systems.[67] As a more ambitious goal, we can also explore the fully resonant regime where $B = U_\gamma$ for some γ for which non-trivial constrained dynamics can arise on fast timescales.[68] Our protocols offer a powerful toolbox for quantum computation and simulation, which is accessible with current state-of-the-art optical lattice experiments, and offers powerful tunability and versatility.

Supporting Information

Supporting Information is available from the Wiley Online Library or from the author.

Conflict of Interest

The authors declare no conflict of interest.

[1] C. Gross, I. Bloch, *Science* **2017**, *357*, 995.
[2] I. Bloch, *Nature* **2008**, *453*, 1016.
[3] T. Calarco, E. A. Hinds, D. Jaksch, J. Schmiedmayer, J. I. Cirac, P. Zoller, *Phys. Rev. A* **2000**, *61*, 022304.
[4] O. Mandel, M. Greiner, A. Widera, T. Rom, T. W. Hänsch, I. Bloch, *Nature* **2003**, *425*, 937.
[5] T. Pellizzari, S. A. Gardiner, J. I. Cirac, P. Zoller, *Phys. Rev. Lett.* **1995**, *75*, 3788.
[6] M. D. Lukin, M. Fleischhauer, R. Cote, L. D. Duan, D. Jaksch, J. I. Cirac, P. Zoller, *Phys. Rev. Lett.* **2001**, *87*, 037901.
[7] K. Eckert, J. Mompart, X. X. Yi, J. Schliemann, D. Bruß, G. Birkl, M. Lewenstein, *Phys. Rev. A* **2002**, *66*, 042317.
[8] E. Charron, M. A. Cirone, A. Negretti, J. Schmiedmayer, T. Calarco, *Phys. Rev. A* **2006**, *74*, 012308.
[9] A. J. Daley, M. M. Boyd, J. Ye, P. Zoller, *Phys. Rev. Lett.* **2008**, *101*, 170504.
[10] M. Anderlini, P. J. Lee, B. L. Brown, J. Sebby-Strabley, W. D. Phillips, J. V. Porto, *Nature* **2007**, *448*, 452.
[11] A. M. Kaufman, B. J. Lester, M. Foss-Feig, M. L. Wall, A. M. Rey, C. A. Regal, *Nature* **2015**, *527*, 208.
[12] M. Mamaev, R. Blatt, J. Ye, A. M. Rey, *Phys. Rev. Lett.* **2019**, *122*, 160402.
[13] C. Weitenberg, S. Kuhr, K. Mølmer, J. F. Sherson, *Phys. Rev. A* **2011**, *84*, 032322.
[14] G. Pagano, F. Scazza, M. Foss-Feig, *Adv. Quantum Technol.* **2019**, *2*, 1800067.
[15] M. Saffman, T. G. Walker, K. Mølmer, *Rev. Mod. Phys.* **2010**, *82*, 2313.
[16] K. Maller, M. T. Lichtman, T. Xia, Y. Sun, M. J. Piotrowicz, A. W. Carr, L. Isenhower, M. Saffman, *Phys. Rev. A* **2015**, *92*, 022336.
[17] M. Saffman, *J. Phys. B: At., Mol. Opt. Phys.* **2016**, *49*, 202001.
[18] A. Negretti, P. Treutlein, T. Calarco, *Quantum Inf. Process.* **2011**, *10*, 721.
[19] H. Levine, A. Keesling, G. Semeghini, A. Omran, T. T. Wang, S. Ebadi, H. Bernien, M. Greiner, V. Vuletić, H. Pichler, M. D. Lukin, *Phys. Rev. Lett.* **2019**, *123*, 170503.
[20] I. S. Madjarov, J. P. Covey, A. L. Shaw, J. Choi, A. Kale, A. Cooper, H. Pichler, V. Schkolnik, J. R. Williams, M. Endres, *arXiv:2001.04455*, **2020**.
[21] Y.-Y. Jau, A. M. Hankin, T. Keating, I. H. Deutsch, G. W. Biedermann, *Nat. Phys.* **2016**, *12*, 71.
[22] Y. Wang, A. Kumar, T.-Y. Wu, D. S. Weiss, *Science* **2016**, *352*, 1562.
[23] M. Endres, H. Bernien, A. Keesling, H. Levine, E. R. Anschuetz, A. Krajenbrink, C. Senko, V. Vuletic, M. Greiner, M. D. Lukin, *Science* **2016**, *354*, 1024.
[24] D. Barredo, S. De Léséleuc, V. Lienhard, T. Lahaye, A. Browaeys, *Science* **2016**, *354*, 1021.
[25] A. Kumar, T.-Y. Wu, F. Giraldo, D. S. Weiss, *Nature* **2018**, *561*, 83.
[26] T. Müller, S. Fölling, A. Widera, I. Bloch, *Phys. Rev. Lett.* **2007**, *99*, 200405.
[27] G. Wirth, M. Ölschläger, A. Hemmerich, *Nat. Phys.* **2011**, *7*, 147.
[28] L. Niu, S. Jin, X. Chen, X. Li, X. Zhou, *Phys. Rev. Lett.* **2018**, *121*, 265301.
[29] P. Soltan-Panahi, D.-S. Lühmann, J. Struck, P. Windpassinger, K. Sengstock, *Nat. Phys.* **2012**, *8*, 71.
[30] C. V. Parker, L.-C. Ha, C. Chin, *Nat. Phys.* **2013**, *9*, 769.
[31] J. Struck, C. Ölschläger, R. Le Targat, P. Soltan-Panahi, A. Eckardt, M. Lewenstein, P. Windpassinger, K. Sengstock, *Science* **2011**, *333*, 996.
[32] D. Hu, L. Niu, S. Jin, X. Chen, G. Dong, J. Schmiedmayer, X. Zhou, *Commun. Phys.* **2018**, *1*, 29.
[33] W. S. Bakr, P. M. Preiss, M. E. Tai, R. Ma, J. Simon, M. Greiner, *Nature* **2011**, *480*, 500.
[34] R. Bücker, J. Grond, S. Manz, T. Berrada, T. Betz, C. Koller, U. Hohenester, T. Schumm, A. Perrin, J. Schmiedmayer, *Nat. Phys.* **2011**, *7*, 608.
[35] D. A. Lidar, I. L. Chuang, K. B. Whaley, *Phys. Rev. Lett.* **1998**, *81*, 2594.
[36] D. Kielpinski, V. Meyer, M. A. Rowe, C. A. Sackett, W. M. Itano, C. Monroe, D. J. Wineland, *Science* **2001**, *291*, 1013.
[37] E. Tiesinga, A. J. Moerdijk, B. J. Verhaar, H. T. C. Stoof, *Phys. Rev. A* **1992**, *46*, R1167.
[38] E. Tiesinga, B. J. Verhaar, H. T. C. Stoof, *Phys. Rev. A* **1993**, *47*, 4114.
[39] C. Chin, R. Grimm, P. Julienne, E. Tiesinga, *Rev. Mod. Phys.* **2010**, *82*, 1225.

[40] M. F. Parsons, F. Huber, A. Mazurenko, C. S. Chiu, W. Setiawan, K. Wooley-Brown, S. Blatt, M. Greiner, *Phys. Rev. Lett.* **2015**, *114*, 213002.

[41] E. Haller, J. Hudson, A. Kelly, D. A. Cotta, B. Peaudecerf, G. D. Bruce, S. Kuhr, *Nat. Phys.* **2015**, *11*, 738.

[42] L. W. Cheuk, M. A. Nichols, M. Okan, T. Gersdorf, V. V. Ramasesh, W. S. Bakr, T. Lompe, M. W. Zwierlein, *Phys. Rev. Lett.* **2015**, *114*, 193001.

[43] A. Omran, M. Boll, T. A. Hilker, K. Kleinlein, G. Salomon, I. Bloch, C. Gross, *Phys. Rev. Lett.* **2015**, *115*, 263001.

[44] G. J. A. Edge, R. Anderson, D. Jervis, D. C. McKay, R. Day, S. Trotzky, J. H. Thywissen, *Phys. Rev. A* **2015**, *92*, 063406.

[45] H. J. Briegel, D. E. Browne, W. Dür, R. Raussendorf, M. Van den Nest, *Nat. Phys.* **2009**, *5*, 19.

[46] R. Raussendorf, D. E. Browne, H. J. Briegel, *Phys. Rev. A* **2003**, *68*, 022312.

[47] S. H. Shenker, D. Stanford, *J. High Energy Phys.* **2014**, *2014*, 67.

[48] J. Maldacena, S. H. Shenker, D. Stanford, *J. High Energy Phys.* **2016**, *2016*, 106.

[49] S. Trotzky, P. Cheinet, S. Fölling, M. Feld, U. Schnorrberger, A. M. Rey, A. Polkovnikov, E. A. Demler, M. D. Lukin, I. Bloch, *Science* **2008**, *319*, 295.

[50] S. Bravyi, D. P. DiVincenzo, D. Loss, *Ann. Phys.* **2011**, *326*, 2793.

[51] I. Dimitrova, N. Jepsen, A. Buyskikh, A. Venegas-Gomez, J. Amato-Grill, A. Daley, W. Ketterle, *arXiv:1908.09870*, **2019**.

[52] M. Gärttner, J. G. Bohnet, A. Safavi-Naini, M. L. Wall, J. J. Bollinger, A. M. Rey, *Nat. Phys.* **2017**, *13*, 781.

[53] A. Mazurenko, C. S. Chiu, G. Ji, M. F. Parsons, M. Kanász-Nagy, R. Schmidt, F. Grusdt, E. Demler, D. Greif, M. Greiner, *arXiv:1612.08436*, **2016**.

[54] R. A. Hart, P. M. Duarte, T.-L. Yang, X. Liu, T. Paiva, E. Khatami, R. T. Scalettar, N. Trivedi, D. A. Huse, R. G. Hulet, *Nature* **2015**, *519*, 211.

[55] M. Boll, T. A. Hilker, G. Salomon, A. Omran, J. Nespolo, L. Pollet, I. Bloch, C. Gross, *Science* **2016**, *353*, 1257.

[56] J. Oreg, F. T. Hioe, J. H. Eberly, *Phys. Rev. A* **1984**, *29*, 690.

[57] K. Bergmann, H. Theuer, B. W. Shore, *Rev. Mod. Phys.* **1998**, *70*, 1003.

[58] S. Al-Assam, R. A. Williams, C. J. Foot, *Phys. Rev. A* **2010**, *82*, 021604.

[59] E. M. Seroka, A. Valdés Curiel, D. Trypogeorgos, N. Lundblad, I. B. Spielman, *Opt. Express* **2019**, *27*, 36611.

[60] F. Scazza, C. Hofrichter, M. Höfer, P. De Groot, I. Bloch, S. Fölling, *Nat. Phys.* **2014**, *10*, 779.

[61] G. Cappellini, M. Mancini, G. Pagano, P. Lombardi, L. Livi, M. S. de Cumis, P. Cancio, M. Pizzocaro, D. Calonico, F. Levi, C. Sias, J. Catani, M. Inguscio, L. Fallani, *Phys. Rev. Lett.* **2014**, *113*, 120402.

[62] J. Ma, X. Wang, Chang-P. Sun, F. Nori, *Phys. Rep.* **2011**, *509*, 89.

[63] A. M. Rey, L. Jiang, M. D. Lukin, *Phys. Rev. A* **2007**, *76*, 053617.

[64] P. Cappellaro, M. D. Lukin, *Phys. Rev. A* **2009**, *80*, 032311.

[65] A. M. Rey, L. Jiang, M. Fleischhauer, E. Demler, M. D. Lukin, *Phys. Rev. A* **2008**, *77*, 052305.

[66] P. He, M. A. Perlin, S. R. Muleady, R. J. Lewis-Swan, R. B. Hutson, J. Ye, A. M. Rey, *arXiv:1904.07866*, **2019**.

[67] X. Li, W. V. Liu, *Rep. Prog. Phys.* **2016**, *79*, 116401.

[68] M. Mamaev, I. Kimchi, M. A. Perlin, R. M. Nandkishore, A. M. Rey, *arXiv:1905.12094*, **2019**.